

Accepted Manuscript

Title: Bifunctional catalysts based on colloidal Cu/Zn nanoparticles for the direct conversion of synthesis gas to dimethyl ether and hydrocarbons

Authors: M. Gentzen, D.E. Doronkin, T.L. Sheppard, J.-D. Grunwaldt, J. Sauer, S. Behrens



PII: S0926-860X(18)30118-2
DOI: <https://doi.org/10.1016/j.apcata.2018.03.008>
Reference: APCATA 16582

To appear in: *Applied Catalysis A: General*

Received date: 21-12-2017
Revised date: 6-3-2018
Accepted date: 13-3-2018

Please cite this article as: Gentzen M, Doronkin DE, Sheppard TL, Grunwaldt J-D, Sauer J, Behrens S, Bifunctional catalysts based on colloidal Cu/Zn nanoparticles for the direct conversion of synthesis gas to dimethyl ether and hydrocarbons, *Applied Catalysis A, General* (2018), <https://doi.org/10.1016/j.apcata.2018.03.008>

This is a PDF file of an unedited manuscript that has been accepted for publication. As a service to our customers we are providing this early version of the manuscript. The manuscript will undergo copyediting, typesetting, and review of the resulting proof before it is published in its final form. Please note that during the production process errors may be discovered which could affect the content, and all legal disclaimers that apply to the journal pertain.

Bifunctional catalysts based on colloidal Cu/Zn nanoparticles for the direct conversion of synthesis gas to dimethyl ether and hydrocarbons

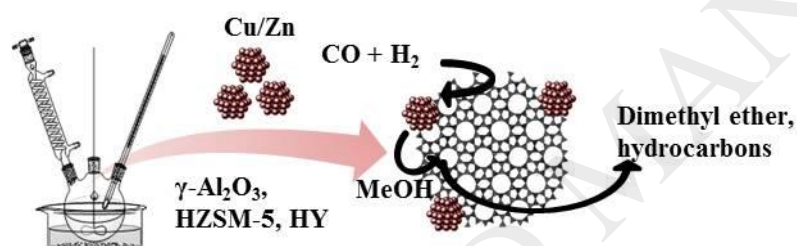
M. Gentzen,^a D. E. Doronkin,^{a,b} T. L. Sheppard,^{a,b} J.-D. Grunwaldt,^{a,b} J. Sauer,^a and S. Behrens^{*a}

^a Institute of Catalysis Research and Technology, Karlsruhe Institute of Technology (KIT), Herrmann-von-Helmholtz-Platz 1, 76344 Eggenstein-Leopoldshafen, Germany; E-mail: silke.behrens@kit.edu

^b Institute for Chemical Technology and Polymer Chemistry, Karlsruhe Institute of Technology (KIT), Engesserstr. 20, 76131 Karlsruhe, Germany

*Corresponding author: silke.behrens@kit.edu

Graphical abstract



Highlights

- Using a model kit principle, well-defined Cu/Zn-based nanoparticle building units are employed for the preparation of specific bifunctional catalysts for syngas conversion to either dimethyl ether or hydrocarbons.
- By this approach, the effects of preparation history are reduced and high comparability of the bifunctional catalysts is enabled.
- Bifunctional catalysts affording the close proximity of two catalytic functions are obtained by subsequently depositing the nanoparticles on different acidic catalysts.
- The formation of the active phase during *in situ* activation is monitored by *in situ* X-ray absorption spectroscopy.
- The present study reveals the importance of Cu loading, Cu to acidic sites ratio and the accessibility of acid sites on the bifunctional catalysts to control activity and selectivity either towards DME or hydrocarbons in the direct conversion of simulated biomass-derived synthesis gas.

Abstract

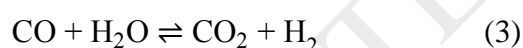
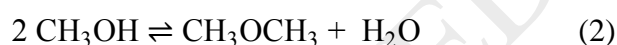
Hybrid catalysts were prepared using well-defined, colloidal Cu/Zn-based nanoparticles as building units. The nanoparticles were immobilized on acidic supports (*i.e.*, γ -Al₂O₃, HZSM-

5, and HY) to yield a series of bifunctional catalysts with a close proximity of active sites for both methanol synthesis and its further conversion to dimethyl ether (DME) or hydrocarbons (HCs). By this model kit principle, a high comparability of the bifunctional catalysts was ensured. The catalysts were characterized in depth regarding their structure and catalytic performance in the conversion of CO-rich synthesis gas. *In situ* XAS studies demonstrated the formation of the active phase under reducing conditions. The present study revealed important material parameters to control activity and selectivity of the bifunctional catalysts either towards DME or liquefied petroleum gas (LPG) products in the direct conversion of simulated biomass-derived synthesis gas. In particular, Cu loading, pore structure and Si:Al ratio were investigated.

Keywords: Single-step dimethyl ether synthesis, nanoparticles, zeolites, bifunctional catalysts

1. Introduction

A promising route to second generation biofuels comprises the conversion of lignocellulosic biomass to synthesis gas *via* gasification, and subsequent upgrading to valuable products.^{1,2} In this context, the syntheses of DME or hydrocarbons *via* the methanol route are particularly interesting. Apart from its direct use for domestic applications or as a clean diesel fuel, DME is applied as an intermediate, *e.g.*, in the production of further base chemicals and gasoline range hydrocarbons. Traditionally, DME is produced from syngas in a two-step process, where methanol is generated over Cu-based catalysts in the first stage, followed by subsequent dehydration over inorganic solid acids (*e.g.*, γ -Al₂O₃ or zeolites) in the second stage. Alternatively, DME can be obtained in a single-step conversion from syngas which involves the following reactions:



In addition, DME production from syngas is thermodynamically favored over methanol and enables higher CO conversions. The overall conversion of syngas-to-DME (STD) is described by Equation 4.



Gasification of biomass-derived feedstocks provides syngas with a H₂:CO ratio in the range of 0.7 to 1.0 which is below the optimum ratio for methanol synthesis (Eq. 1).^{2,3} In the present study, CO-rich syngas (CO:H₂ ratio 1:1) was employed to simulate biomass-derived feedstocks for the STD process (Eq. 4).

The STD process has many technical and economic advantages, provided that a suitable catalyst exists. Typically, the two catalysts are combined by simple physical mixing.^{4,5} Cu/ZnO (Al₂O₃) is industrially applied as a catalyst in methanol synthesis and has also been

used as the methanol active component in the STD process for several years.^{6,7,8} The ideal solid acid catalyst for methanol dehydration should exhibit appropriate acid sites, high stability, hydrophobic surface, low cost, high activity, and good selectivity for the desired products. In particular, alumina and zeolites have been employed for methanol dehydration to DME.^{9,10,11,12,13} γ -Al₂O₃ is known as a very efficient dehydration catalyst with high DME selectivity, low cost, excellent lifetime, and high mechanical resistance. The surface of γ -Al₂O₃ remains with an excess of positive charge which is compensated by hydroxyl anions (OH⁻). The hydroxyl anions form weakly acidic sites but desorption at high temperatures creates coordinatively unsaturated metal cations and oxygen anions that can act as Lewis acid and base sites, respectively. Although the cubic, defect spinel-type γ -Al₂O₃ reveals a remarkable selectivity to DME, zeolites have been reported to exhibit a better catalytic activity and stability. In this context, H-ZSM-5 is of particular interest since it combines strong acidity, high density of acid sites and medium size pores which prevent coking without significantly hindering the diffusion of molecules involved in the DME synthesis. In zeolites, the number of acid sites for methanol dehydration can be further adjusted *via* the Si/Al ratio. In contrast to γ -Al₂O₃, molecular sieves (*e.g.*, SAPO-34, HY, H-ZSM-5) can be further employed in hybrid catalysts for the production of hydrocarbons from syngas where, due to a so-called “drain-off” mechanism, no thermodynamic constraints are imposed on the overall syngas feed conversion.

The design of catalysts remains a crucial issue for enhancing catalytic efficiency. In the STD process, the large distance between the two catalytically active sites, a rather low activity, and low long-term stability have been described as the major drawbacks of physically mixed catalytic systems.¹⁴ Diffusion of intermediates (*e.g.* methanol) through the interface between methanol synthesis catalyst and acid functions are an essential part of the reaction scheme and synergistic effects were observed for single bifunctional entities, if the two catalytically active components were finely dispersed and maintained in close contact.^{15,16} A conventional bifunctional catalyst can be prepared by mixed metal impregnation, co-precipitation impregnation, or co-precipitation sedimentation of the dehydration catalyst.^{15,16,17,18} However, the features and activity of the bifunctional catalyst strongly depend on the preparation history. They often exhibit complex structures with broad size and shape distributions of the active particles impeding fundamental studies on the influence of the various structural parameters on the catalytic performance.^{19,20} In this context, catalysts derived from well-defined nanoparticle building units may help to reduce this complexity and to contribute to a more fundamental understanding.^{20,21} Colloidal nanoparticles have been employed as quasi-homogeneous catalysts for liquid-phase methanol and DME synthesis by dispersing the nanoparticles in the reaction medium.^{22,23,24,25,26} Here, long-chain surfactants or ligands are typically adsorbed on the nanoparticle surface to prevent agglomeration, which influences the catalytic properties of the particles. Following the precursor concept, the nanoparticles are immobilized on the support and subsequently converted into heterogeneous catalysts with a nanoscale proximity of the particles and the support.^{27,28,29}

In general, catalyst studies can often suffer from limited comparability due to differences in their preparation history. Preparation of catalysts typically requires individually optimized synthetic recipes, and the resulting differences in homogeneity, dispersion etc. may

additionally complicate the comparison of the catalyst performance. In our approach, the bifunctional catalysts were prepared based on well-defined, colloidal nanoparticle building units, thus providing a flexible toolkit to minimize the influence of differences in preparation histories. Uniform nanoparticles obtained *via* a colloidal, organometallic approach were employed as a precursor for the methanol active component and subsequently supported on a solid acid, namely γ -Al₂O₃ and zeolites of different acidity (*i.e.*, HZSM-5, HY with varying Al/Si ratio). This versatile approach to produce bifunctional model catalysts allowed a comparative study of the respective dehydration catalysts in the conversion of syngas. In particular, the effects of Cu loading, pore structure and Si:Al ratio were investigated. The catalysts were characterized by scanning electron microscopy (SEM) with energy dispersive X-ray spectroscopy (EDX), ammonia desorption (NH₃-TPD), N₂-physisorption, temperature-programmed reduction (H₂-TPR), X-ray diffraction (XRD), and *in situ* and *operando* X-ray absorption spectroscopy (XAS). The catalytic performance was evaluated in a continuously operated laboratory scale plant using simulated biomass-derived synthesis gas between 250 and 300 °C and correlated with structural parameters of the bifunctional catalysts.

2. Experimental

2.1 Materials

All chemicals were used without further purification. Unless specified otherwise, all nanoparticle synthesis steps were carried out under argon atmosphere and water-free conditions. Copper(II) acetylacetonate (Cu(acac)₂, Sigma Aldrich, $\geq 99.9\%$ trace metal basis), diethylzinc ((C₂H₅)₂Zn, Sigma Aldrich, ≥ 52 wt.-% Zn), toluene (Sigma Aldrich, 99.8%), ethanol (VWR, absolute) were used for nanoparticle synthesis. Zeolites (ZSM-5: CBV3024E, CBV 5524G, CBV 28014 (nominal cation form ammonium); HY: CBV 720), AEROSIL® 150, and γ -Al₂O₃ were obtained from Zeolyst International, Evonik, and Alfa Aesar, respectively. Gases (CO 3.7, H₂ 6.0, Ar 6.0, N₂ 6.0) were obtained from Air Liquide.

2.2 Synthesis of Cu/Zn-based nanoparticles

Cu/Zn-based nanoparticles were synthesized according to a procedure previously described by us.²⁹ Briefly, (C₂H₅)₂Zn (12 mL, 1.2 M in toluene) was slowly added to Cu(acac)₂ (10.49 g, 40 mmol, suspended in 800 mL toluene) over a period of 90 min at 40 °C and stirred at 40 °C for 24 h. Eventually, all volatile components were removed, and the product was dried in vacuum. Cu/Zn-based nanoparticles (mean particle diameter as determined by TEM analysis: 6.2 \pm 2.0 nm) were obtained as a black powder and further used for the preparation of the bifunctional catalysts.

2.3 Preparation of bifunctional catalysts

The following solid acids were used as both support for the immobilization of the Cu/Zn nanoparticles and methanol dehydration catalyst: γ -Al₂O₃, ZSM-5 zeolites with increasing Si/Al ratio (*i.e.*, 15 (CBV3024E), 25 (CBV 5524G), 140 (CBV 28014), and zeolite Y (Si/Al ratio 15 (CBV 720)). As a reference, the Cu/Zn nanoparticles were also supported on pure silica (AEROSIL® 150) and physically mixed with the methanol dehydration catalyst (CBV 5524G). Before use, all solid acids were calcined. During the calcination procedure, they were

initially heated to 120 °C (heating rate 2 °C/min), which was maintained for 3 h. The temperature was then raised to 550 °C (heating rate 3 °C/min) and maintained for 4 h. After calcination, the powders were evacuated for at least 12 h and stored under argon. The bifunctional catalysts were prepared by suspending the dried Cu/Zn-based nanoparticles with the calcined dehydration catalysts in weight ratios between 1:1 and 4:1 in toluene (50 mL) while stirring for 15 min. The solvent was subsequently removed in vacuum, and the resulting bifunctional catalysts were again calcined at 350 °C for 4 h (heating rate 110 °C/h) to remove any organic residues from nanoparticle synthesis. Finally, the catalysts were pelletized, crushed, and sieved to the fraction of 80 to 160 μm . All catalysts are denoted as follows: CZ (X)-Y (Z) where CZ is a bifunctional catalyst derived from Cu/Zn-based nanoparticles, X the Cu loading [wt.-%], Y the type of solid acid with A ($\gamma\text{-Al}_2\text{O}_3$), HZSM-5, or HY, and Z the Si/Al ratio of the zeolite. “CZ (7)-HZSM5 (15)”, for example, corresponds to a bifunctional catalyst based on Cu/Zn nanoparticles, with 7 wt.-% Cu loading on HZSM-5 with Si/Al ratio of 15.

2.4 Characterization

SEM-EDX investigations were carried out on the bifunctional bulk catalysts with a DSM 982 Gemini SEM, equipped with a Schottky-type thermal field emission cathode (Zeiss corp., Germany) and an EDX spectrometer. The total specific surface area of the catalysts was determined with N_2 -physisorption experiments and the Brunauer Emmet Teller (BET) method using a Quantachrome Nova 2000e instrument. The samples were initially dried at 230 °C for 12 h. Powder XRD patterns were recorded on a PANalytical X'Pert Pro X-ray diffractometer employing a Bragg-Brentano geometry with Cu $K\alpha$ radiation and a Ni filter. The range between 5° and 120° (2θ) was measured within 1 h. The diffraction peaks were compared to reference compounds reported in the Joint Committee of Powder Diffraction Standards (JCPDS) data base. The crystallite size d was estimated based on the reflections at 43° and 39° (2θ) for the Cu and the CuO phase, respectively, according to the Scherrer equation

$$d = \frac{0.9 \lambda}{\beta \cos(\theta)} \quad (5)$$

where 0.9 is the shape factor, β the full width at half maximum of the diffraction peak, and θ the Bragg angle. LaB_6 (NIST) was used as a standard in order to account for instrumental line broadening. To evaluate the acidic properties of the activated, reduced bifunctional catalyst, TPR and TPD measurements were conducted consecutively on the same catalyst. For TPR measurements, the calcined catalyst (at least 150 mg) was initially dried in an Ar stream (30 mL/min, heating rate 5 °C/min, 300 °C, 120 min), and the reduction behavior subsequently analyzed from 50 °C to 250 °C in a reducing gas stream (2 vol.-% H_2 in Ar, heating rate 2 °C/min) with a Micromeritics AutoChem HP 2950. Following these TPR experiments, programmed desorption TPD measurements were performed on the same, reduced catalyst sample. Therefore, the catalysts were cooled to 100 °C and NH_3 (1.221 ± 0.024 vol.-% NH_3 in He, 30 mL/min) was subsequently loaded for 60 min. Desorption of NH_3 was recorded with a mass spectrometer (MS, MKS Cyrrus) from 120 °C to 750 °C (heating rate 4 °C/min).

In situ XAS spectra were measured at the CAT-ACT beamline of the KIT synchrotron radiation source (KIT, Karlsruhe) in fluorescence mode using a PIPS diode at Cu K edge and

transmission mode at Zn K edge.³⁰ The incident energy was selected by a double crystal monochromator with a pair of Si (111) crystals to scan energies around Cu K and Zn K edges. Higher harmonics were rejected by a pair of Si coated mirrors. The beam size at the sample was set to 1 (horizontal) \times 0.5 (vertical) mm². The catalyst (6 mg, diluted 4 times (by weight) with γ -Al₂O₃) was placed in an *in situ* microreactor (quartz capillary, 1.5 mm diameter, 20 μ m wall thickness, catalyst bed length approx. 5 mm) between two quartz wool plugs and mounted horizontally over a hot air blower (FMB Oxford GSB-1300).³¹ The temperature was calibrated using an external thermocouple at the top and the bottom of the capillary microreactor without X-ray beam. He or 5 vol.% H₂/He were dosed using individual mass flow controllers (Bronckhorst) at a flow rate of 50 mL/min, and the gas was analyzed at the outlet using a Pfeiffer Vacuum OmniStar GSD320 mass spectrometer. X-ray absorption near-edge structure (XANES) and extended X-ray absorption fine structure (EXAFS) spectra were initially recorded at 25 °C in a He flow. The gas mixture was then switched to 5 % H₂/He, and XANES spectra were recorded continuously during heating to 250 °C (heating rate 1 °C/min). At 250 °C and 5 % H₂/He flow, several XANES and EXAFS spectra were recorded over a period of 60 min. Next, synthesis gas was introduced to the *in situ* microreactor (15 vol.-% H₂, 15 vol.-% CO in He, 250 °C, 18 mL/min, 3 bar) and maintained for one hour. During the test under synthesis gas, XANES spectra were continuously recorded and an additional set of EXAFS spectra at the Cu and Zn K edges was recorded after 1 h time on stream. The spectra were normalized and background subtracted to extract EXAFS data using the ATHENA program from the IFFEFIT software package.³² The average oxidation state of Cu and Zn was determined by a Linear Combination Analysis (LCA) using reference spectra of the corresponding metal foils and metal oxides. The k¹-, k²-, and k³-weighted EXAFS functions were Fourier transformed in the k range of 3.0 to 11 Å⁻¹ and multiplied by a Hanning window with sill size of 1 Å⁻¹. The structural models were based on bulk Cu metal (Inorganic Crystal Structure Database, ICSD collection code 43493) and wurtzite ZnO (ICSD collection code 26170). Structure refinement was performed using ARTEMIS software (IFFEFIT).³² For this purpose, the theoretical backscattering amplitudes and phases were calculated by FEFF 6.0,³³ then adjusted to the experimental spectra by a least square method in R-space between 1.5 and 2.9 Å⁻¹ (Cu K) and between 1.0 and 4.0 Å⁻¹ (Zn K). First, the amplitude reduction factors were calculated using the Cu foil and ZnO reference spectra, and then, the coordination numbers, interatomic distances, energy shifts (δE_0), and mean square deviations of interatomic distances (σ^2) were refined. The absolute misfit between theory and experiment was expressed by ρ .

2.5 Catalytic testing

The catalytic properties were evaluated in a continuously operated laboratory scale plant equipped with a plug flow reactor. Gases (CO, H₂, Ar, N₂) were dosed using mass flow controllers (Bronckhorst), and effluent gases were analyzed with a gas chromatograph (Hewlett Packard 6890). Two different columns (RESTEK RT®-U-Bond, RESTEK RT-Msieve) as well as two detectors (thermal conductivity detector, flame ionization detector) were employed to analyze the gas mixtures. Before the catalytic tests, mass and heat transfer limitations were excluded for each reaction temperature using the EUROKIN webtool. Properties of the gas mixture (e.g. viscosity) were calculated using ASPEN plus. Before

catalytic testing, the calcined catalyst (2 g) was activated *in situ* using the following reduction procedure: (1) heating (rate 17 °C/h) in 2 vol.-% H₂ in Ar (100 mL_{NTP}/min (normal temperature and pressure (NTP): 0 °C, 1 atm)) to 200 °C, (2) 1 h at 200°C (2 vol.-% H₂ in Ar), (3) heating (rate 17 °C/h) to 240 °C (2 vol.-% H₂ in Ar), (4) 1 h at 240°C (2 vol.-% H₂ in Ar), (5) heating (rate 10 °C/h) in pure H₂ (50 mL_{NTP}/min) to 250 °C, and (6) 1 h at 250°C (H₂). Subsequently, the reactor was pressurized to 50 bar, and the educt gases were introduced (total flow 50 mL_{NTP}/min, Ar:N₂:H₂:CO = 5:2:1.5:1.5). The composition of the reactant feed stream was adjusted by independent mass flow controllers placed on the flow lines of each reactant gas (Ar, N₂, H₂, CO). The temperature was increased every 6 h by 10 °C (heating rate 10 °C/h) until the final temperature of 300 °C was reached. The catalytic performance was evaluated using the following equations:

$$X_{\text{CO}} = \frac{\dot{N}_{\text{CO},0} - \dot{N}_{\text{CO}}}{\dot{N}_{\text{CO},0}} \cdot 100 \quad (6)$$

where $\dot{N}_{\text{CO},0}$ is the molar flow rate of carbon monoxide at reactor inlet, \dot{N}_{CO} the molar flow rate of carbon monoxide at reactor outlet and X_{CO} the CO-conversion in %;

$$S_i = \frac{\xi_i(\dot{N}_i - \dot{N}_{i,0})}{\dot{N}_{\text{CO},0} - \dot{N}_{\text{CO}}} \cdot 100 \quad (7)$$

where S_i is the selectivity of component i , \dot{N}_i the molar flow rate of component i at reactor outlet, $\dot{N}_{i,0}$ the molar flow rate of component i at reactor inlet and ξ_i the number of carbon atoms in a molecule of component i . Selectivities of higher hydrocarbons ($\geq C_5$) could not be determined by Equation 7 and were summarized as S_{C5+} calculating the residual carbon selectivity.

The DME yield (Y) was calculated according to Equation 8.

$$Y_i = X_{\text{CO}} \cdot S_i \quad (8)$$

3. Results and discussion

3.1 Catalyst preparation and characterization

Well-defined Cu/Zn-based nanoparticles were employed as precursors for the methanol active component and successively supported on a solid acid to yield a series of bifunctional catalysts exhibiting close proximity of the two catalytically active sites.

By this model kit principle, a high comparability of the respective bifunctional catalysts was ensured (Figure 1). The reaction of (C₂H₅)₂Zn with Cu(acac)₂ yielded well defined, uniform Cu/Zn-based nanoparticles with a narrow size distribution. The synthesis and the structure of the Cu/Zn-based nanoparticles were previously described in detail.²⁹ This procedure was not only highly reproducible but could be easily scaled up in a single batch experiment to yield the quantity of nanoparticles necessary to carry out several catalyst tests. Based on TEM analysis, the Cu/Zn-based nanoparticles were 6.2 (±2.0) nm in size. The nanoparticle building units were subsequently immobilized on the solid acid (*i.e.*, γ -Al₂O₃, HZSM-5, HY) to yield

the dual site catalysts. A series of bifunctional systems was prepared on HZSM-5 increasing the Si/Al ratio from 15, 25 to 140 and the Cu loading from 7 to 15 wt.-%. For all catalysts, the molar Cu/Zn ratio was approximately 1:3. As a reference, the Cu/Zn-based particles were supported on pure silica (*i.e.*, AEROSIL® 150) and physically mixed with HZSM-5 (Si/Al ratio 25). Table 1 summarizes the composition and the specific total surface areas (A) of the bifunctional catalysts. The specific surface areas of the catalysts decreased with increasing metal loading and, thus, simultaneously decreasing support fraction. Due to the small pore size of the zeolites (HZSM-5 0.51 to 0.56 nm, HY 0.74 nm),³⁴ the 6 nm-sized Cu/Zn particles are deposited on the outer surface of the support which may result in a partial blockage of the micropores. In order to account for the different CuO/ZnO/support fractions and to compare the effect of particle deposition in the different catalysts, the BET surface area (A_{BET}) of the individual components were weighted by their fraction in the final catalyst according to Equation (8).

$$A_{\text{calculated}} = w_{\text{support}} \cdot A_{\text{support}} + w_{\text{MeOH cat}} \cdot A_{\text{MeOH cat}} \quad (8)$$

where w_{support} is the zeolite content (wt.-%), A_{support} the specific surface area of the support (according to manufacturer, m^2/g), $w_{\text{MeOH cat}}$ the content of methanol active component (wt.-%), and $A_{\text{MeOH cat}}$ the specific surface area of the calcined Cu/Zn-powder without support ($31 \text{ m}^2/\text{g}$ as determined by N_2 -physisorption). In general, the experimental BET surface areas were in good agreement with the calculated values, indicating that deviations in BET surface areas resulted from different weight fractions of the two catalytically active components. For the catalysts with a high Cu loading (13 wt.-%), however, the theoretical and experimental surface areas differed significantly ($> 10\%$ relative), suggesting partial micropore blockage of the supports by Cu/Zn nanoparticles.

The catalysts were investigated by powder XRD before and after catalytic testing. XRD patterns of the calcined bifunctional catalysts are shown in Figure 2.

The XRD patterns showed the reflections of both the hexagonal ZnO phase (JCPDS 01-089-0510) and the monoclinic CuO phase (JCPDS 01-089-5898), whereas no indication for the formation of any mixed oxide species or alloyed Cu_xZn_y phases were observed. Depending on the acidic support, the bifunctional catalysts additionally revealed the reflections of the cubic $\gamma\text{-Al}_2\text{O}_3$ phase (JCPDS 00-010-0425), the orthorhombic HZSM-5 phase (JCPDS 00-044-0003), or the cubic HY phase (JCPDS 01-077-1551). The diffraction patterns displayed broad reflections indicating small crystallite sizes, which were estimated using the Scherrer equation (Equation (5), Figure S1). All catalysts revealed CuO crystallite sizes in the range of 11 nm and 19 nm indicating a growth of the initial, 6 nm-sized Cu/Zn-based nanoparticles during the calcination step. After catalytic testing, the STD catalysts were isolated under inert conditions and characterized using XRD. The corresponding patterns (Figure S2) showed again reflections of the hexagonal ZnO phase (JCPDS 01-089-0510) and the respective dehydration catalyst. The relative intensity of the wurtzite ZnO reflections decreased after the catalyst tests, suggesting the formation of some amorphous ZnO species.³⁵ All catalysts revealed the reflections of the metallic Cu phase (JCPDS 01-089-2838). No reflections of a CuO phase,

alloyed Cu_xZn_y phases or a reduced Zn phase were observed. According to the Scherrer equation, the Cu crystallite sizes ranged from 28 nm to 45 nm and were in a similar size range for all bifunctional catalysts (Figure S1). Copper has a low Hüttig temperature which is reflected by a relatively low melting point (*i.e.*, bulk Cu 1083 °C), thus Cu catalysts have to be operated at relatively low temperatures. Usually methanol synthesis is conducted at pressures of 50 to 100 bar and temperatures of 240 to 260 °C, accordingly. Higher temperatures up to 300 °C may already cause severe sintering of the Cu/Zn nanoparticles.

H_2 -TPR measurements were carried out to investigate the reduction behavior of the calcined catalysts. The H_2 -TPR profiles of the catalysts showed a main reduction peak with shoulders below 250°C (Figure S3). Multiple peaks were assigned to the consecutive reduction of CuO over Cu_2O to Cu,³⁶ or to the reduction of different Cu species, where the finely dispersed or near-surface Cu species were reduced at lower temperatures than bulk Cu.^{37,38} Furthermore, the formation of spinel-type metal oxides (*e.g.*, CuAl_2O_4) or the strong interaction of ZnO and CuO have been discussed.^{39,40} In this study, both the Cu loading and the Si/Al ratio of the supports influenced the reduction temperature. In general, a higher Cu loading led to an increase in the reduction temperature. The main reduction peaks of the HZSM-5 (140)-based bifunctional catalysts, *e.g.*, were shifted from 185 °C (7 wt.-% Cu loading) to 203 °C (13 wt.-% Cu loading). The effect of the metal loading on the reduction temperature was also described by others.⁴¹ A minimum in reduction temperature of approximately 180 °C was observed for 6 wt.-% Cu on $\gamma\text{-Al}_2\text{O}_3$, whereas higher and lower Cu loadings resulted in a shift of the reduction peak to higher temperatures, where shoulders appeared at >250 °C. The interaction of the colloidal nanoparticles with the support may have further influenced the distribution of the particles on the support during the immobilization step. Hence, the formation of nanoparticle multilayers on the supports may additionally result in a shift of the reduction temperatures.

The formation of the active phase was monitored for CZ (12)-A using *in situ* XAS experiments. The XANES spectra at the Cu K and Zn K edge recorded during the activation procedure are shown in Figure 3. During *in situ* activation, CuO underwent a fast reduction to Cu at approximately 135 °C without any significant Cu(I) formation. The sharp reduction behavior indicated a narrow size distribution of the Cu/Zn particles. The XANES spectra at the Cu K edge confirmed the complete reduction of CuO to Cu nanoparticles at temperatures below 250 °C. This was further supported by the EXAFS spectrum of the activated catalyst at the Cu K edge revealing a Cu-Cu distance of 2.53 ± 0.01 Å in good agreement with the bulk Cu reference (2.543 ± 0.003 Å) (Figure S4, Table S1). Zn^{2+} did not change its oxidation state, excluding the formation of reduced Zn^0 species or a Cu/Zn alloy, accordingly (Figures 3b and S4).

The formation of alloyed Cu/Zn catalysts has been previously described by others.⁴² In agreement with our XAS experiments, the instability of CuZn species ((111) surface) under typical conditions of methanol synthesis and the formation of ZnO species was reported by Kattel et al.⁴³ The EXAFS spectra at Zn K edge (Figure S4, Table S2) further didn't show any reduced Zn species or Cu_xZn_y alloy formation. Only Zn-O and Zn-Zn distances which were consistent with the bulk ZnO reference were observed. However, the backscattering intensity corresponding to the second shell in both calcined and reduced CZ (12)-A was significantly

lower than in the hexagonal (wurtzite) ZnO reference (*i.e.*, 6 Zn neighbors compared to 12 Zn in bulk ZnO). This corresponds to the theoretical structure of graphitic ZnO.⁴⁴ Recently, the formation of metastable “graphite-like” ZnO layers during reductive activation was reported for industrial Cu/ZnO/Al₂O₃ catalysts induced by strong metal–support interactions.³⁵ Previous studies have also suggested the formation of oxygen vacancy sites in ZnO, depending on the reactive conditions over the catalyst.⁴⁵ However, taking into account the unchanged first shell (4 O atoms) interatomic distances and the full set of XRD reflections corresponding to the bulk ZnO, the change in the EXAFS spectra at Zn K edge rather suggested the formation of hexagonal ZnO with a high amount of Zn vacancies. The number of Zn vacancies significantly increased following the reductive pretreatment (Table S2). This was in good agreement with the decrease in the relative intensities of the ZnO reflections observed by XRD analysis after the catalyst tests.

After 1 h under synthesis gas (15 vol.-% H₂, 15 vol.-% CO in He, 250 °C) at 3 bar no differences in the XANES spectra at Cu K edge were observed, implying no change in the oxidation state or structure of Cu. A slight increase in the backscattering amplitude of the first shell was observed in the Cu K EXAFS spectrum (Figure S4), which was attributed to slightly higher average Cu coordination number than in the activated sample (Table S1). This difference may point to some increase in the size of Cu nanoparticles under synthesis gas. Small changes were observed also in the XANES (slight decrease of the white line, not shown) and EXAFS spectra (Figure S4, Table S2) at Zn K edge. Considering that no peak at 2.4 Å (corresponding to metallic Zn, uncorrected for the phase shift) appeared, exposure of CZ (12)-A to the synthesis gas feed led to further amorphization of ZnO. This conclusion is supported by significantly higher disorder in the coordination environment around Zn atoms (higher Debye-Waller factors and error bars).

The acidity of zeolites has been identified as an important parameter to determine the catalytic performance of the STD reaction.¹⁰ In zeolites, the acidic properties depend on the amount of framework aluminium. Hence, it can be tuned by varying the Si/Al ratio which affects the catalytic activity and hydrothermal stability. The acidic properties of the bifunctional catalysts were investigated by NH₃-TPD using the reduced catalyst samples after the H₂-TPR experiments (Figure S5). Both the total specific amount of desorbed ammonia and the fraction of strong acid sites (desorption temperature above 500 °C) were determined for the bifunctional catalysts (Table 2). For all bifunctional catalysts, the specific amount of desorbed NH₃ decreased with respect to the acidic supports. As expected, the pure silica support (AEROSIL® 150) did not reveal any acid sites. The Cu/Zn nanoparticles supported on silica (CZ (9)-AEROSIL), however, featured some desorbed NH₃ (81.9 μmol_{NH3}/g_{cat}). This demonstrates that, for all catalysts, a fraction of the desorbed NH₃ has in fact to be assigned to an interaction of NH₃ with the Cu nanoparticles. This is not surprising since Cu is known to coordinate NH₃ to form a variety of amine complexes.

In previous studies, the unexpected increase of desorbed NH₃ for bifunctional STD catalysts was ascribed to interactions between the two catalytically active components. Flores et al. observed both an increase in the number of acid sites due to the formation of new acid sites by Al species and a decrease of this amount due to the blockage of pores.⁴⁶ ZnO is known to display basic O²⁻ sites which may be naturalizing some acid sites. Moreover, migration and

ion exchange of Cu^{2+} species with the hydroxyl groups was shown to lead to a decrease in the concentration of zeolite Brönsted acid sites and has been considered as a potential mechanism for the deactivation of STD catalysts during reaction.⁴⁷ Selective neutralization of Brönsted acid sites on the outer zeolite surface (e.g., using TEOS), however, was shown to slow down copper sintering and migration and resulted in the better catalyst stability and slightly higher selectivity to DME. Based on the experimental TPD results of the pure dehydration catalysts and CZ (9)-AEROSIL, the theoretically expected amount of desorbed NH_3 was calculated according to Equation 9.

$$N_{\text{NH}_3, \text{calculated}} = x_{\text{support}} \cdot N_{\text{NH}_3, \text{support}} + x_{\text{Cu}} \cdot N_{\text{NH}_3, \text{Cu}} \quad (9)$$

with $N_{\text{NH}_3, \text{Cu}} = 880.6 \mu\text{mol/g}_{\text{Cu}}$ (calculated from $N_{\text{NH}_3, \text{CZ (9)-AEROSIL}} \cdot x_{\text{Cu, CZ (9)-AEROSIL}}^{-1}$).

Within the experimental error, the theoretical number of acid sites was in good agreement with the experimental data. For catalysts with 13 wt.-% Cu loading, however, the expected amount of desorbed NH_3 was significantly higher than the experimentally observed values, most probably indicating a reduced accessibility of acid sites *via* the partial blockage of micropores by Cu/Zn nanoparticles. This is also in good agreement with N_2 -physisorption experiments.

3.2 Catalytic performance

The catalysts were activated *in situ* in the reactor as described above and tested in a continuously operated, laboratory scale plant for the single-step conversion of simulated, biomass-derived synthesis gas ($\text{H}_2:\text{CO} = 1:1$) to dimethyl ether and hydrocarbons. In all experiments, pressure (50 bar) and inert gas dilution (70% inert gas dilution) were kept constant, and the temperature was varied between 250°C and 300°C. Nitrogen was used as an internal standard. In particular, the influence of reaction temperature, Cu loading, type of solid acid, pore structure and Si:Al ratio on CO conversion and DME selectivity was investigated.

3.2.1 Influence of the reaction temperature

The bifunctional catalysts were tested at reaction temperatures ranging from 250 °C to 300 °C. When $\gamma\text{-Al}_2\text{O}_3$ was used as support, maximum CO conversions which were consistent with the thermodynamic equilibrium (*i.e.*, according to Equation 4) were obtained (Fig. S6). In this case, DME was the main reaction product with selectivities between 65 % (250 °C) and 55 % (300 °C). At higher reaction temperatures, the zeolite-based bifunctional catalysts yielded higher CO conversions (*i.e.*, as compared to thermodynamic equilibrium) since methanol or DME were continuously withdrawn by the formation of hydrocarbons (Fig. S6). Here, short chain paraffins up to C_4 , methylated alkanes (up to C_7) and benzenes (up to C_{12}) were obtained. In contrast to the conventional methanol-to-gasoline (MtG) process, no alkenes were formed due to the high H_2 partial pressure resulting in a complete hydrogenation of any alkene intermediates over the methanol active component, which has also been observed by others.^{48, 49}

3.2.2 Influence of the metal loading

A series of bifunctional systems was prepared with Cu loadings from 7 to 13 wt.-%. The influence of the metal loading is shown exemplarily for the HZSM-5 dehydration catalyst with a Si/Al ratio of 140:1 in Figure 4.

In general, a higher metal loading (*i.e.*, a higher fraction of the methanol catalyst) led to both a higher CO conversion and a higher DME yield. At 250 °C, DME was the main reaction product for HZSM-5 (140)-based catalysts with selectivities between 62 % and 66 %. This agrees well with the DME selectivity expected for the STD process (Equation 4). Moreover, at 250°C, the CO conversion increased linearly with the Cu loading, further demonstrating the benefit of our uniform Cu/Zn-based nanoparticles as precursors for the methanol active component and the reduced influence of the preparation history.

The increase in reaction temperature, however, led to a sharp decline in DME yield due to the formation of hydrocarbons *via* the MtG process. For lower Cu loadings and therefore higher amount of zeolite and acidic sites in the bifunctional catalysts, hydrocarbon formation was shifted towards lower temperatures (Figure 4). A similar trend was observed for the Cu/Zn nanoparticles supported on HZSM-5 with Si/Al ratios of 15 and 25 (Figure S7). The formation of higher hydrocarbons from N₂/methanol mixtures has been described on HZSM-5 catalysts upon repeated flow through the catalyst bed by Choudry et al.⁵⁰ A higher hydrocarbon selectivity was also reported by Chang et al. in the MtG process with increasing residence time.⁵¹ Moreover, catalysts with lower Cu loading showed lower CO conversions, and therefore, a higher CO partial pressure. The formation of the first C-C bond from methanol under He and CO flow was investigated by Liu et al. While there was no olefin-formation under helium, the authors observed the formation of olefins under CO flow.⁵² Overall, a well-balanced mixing ratio of the two catalytically active components represents a crucial issue for the catalytic performance of these bifunctional systems.

3.2.3 Influence of the dehydration catalyst

To determine the influence of the dehydration component, the Cu/Zn nanoparticles were further immobilized on γ -Al₂O₃, HY and HZSM-5 (Si/Al ratio of 15) to yield a series of bifunctional catalysts (*i.e.*, 12 wt.-% Cu loading). In Figure 5, the DME yield is shown as a function of the reaction temperature. The γ -Al₂O₃-based catalyst revealed a DME yield of 25 % (280 °C) and thus, the highest DME yield among these dehydration catalysts (Figure 5, left).

Due to the weakly acidic sites of γ -Al₂O₃, only methane was formed as a by-product at temperatures above 290 °C. The methane selectivity was 5.5 % and 8.8 % at 290 °C and 300 °C, respectively. For HZSM-5 and HY, the acidity depends not only on the number of framework aluminum species but also on the structure of the crystalline microporous zeolite framework. As shown by NH₃-TPD experiments (Table 2), the HZSM-5-based bifunctional catalysts had not only a higher total number of acid sites but also more strong acid sites (NH₃ desorption > 500 °C) than the HY-based catalyst. Despite the lower total number of acid sites and less strong acid sites, hydrocarbon formation occurred already at temperatures as low as 250 °C for CZ (12)-HY (15) as indicated by a lower DME yield. In addition to the total

number and strength of the acidic sites, however, the different pore sizes (HY: 0.74 nm, HZSM-5 0.51-0.56 nm) and specific surface areas of the two acid catalysts (HY: 780 m²/g, HZSM-5: 405 m²/g) need to be considered, affecting the accessibility of acid sites and thus, the catalytic properties of the bifunctional systems.

In another experiment, the number of framework aluminum species was increased using HZSM-5-based zeolites with Si/Al ratios of 140, 25, and 15. The Cu/Zn-based nanoparticles were successively immobilized on these HZSM-5 zeolites to yield a series of bifunctional catalysts with a Cu loading of 13 wt.-%. (Figure 5, right). HZSM-5 (140) showed both the highest DME yield (*i.e.*, Y_{DME} 25 % at 280 °C) and the highest CO conversion (*i.e.*, X_{CO} 40 % at 280 °C) for temperatures of up to 290 °C, which suggests a balanced composition of the individual active components in the bifunctional catalyst with respect to the STD reaction. No significant influence on the CO conversion was reported for HZSM-5 zeolites with varying Si/Al-ratios by Kim et al., as long as methanol synthesis was the rate determining step in the STD reaction.⁵³ In this study, the methanol selectivities were below 2.6 %, and, thus, methanol synthesis was considered the rate determining step. Here, the highest CO conversion was observed for the HZSM-5-based catalyst with the lowest amount of Al species (Si/Al ratio 140). At 300 °C, CO conversion (*i.e.*, X_{CO} 47 %) was the highest among all bifunctional catalysts. The selectivity to C₁-C₄ hydrocarbons was 28.9 % for (56.3 % of hydrocarbon products), whereas CZ (13)-HZSM-5 (25) and CZ (13)-HZSM-5 (140) displayed 19.8 % (37.5 % of hydrocarbon products) and 18.2 % (39.2 % of hydrocarbon products), respectively.

Interestingly, CZ (13)-HZSM-5 (25) revealed the lowest temperature for hydrocarbon formation, although CZ (13)-HZSM-5 (15) had a higher total number and more strong acid sites. SEM images of the pristine supports are displayed in Figure S8. As compared to the other dehydration catalysts, it is obvious from these images that this zeolite (*i.e.*, HZSM-5 (25)) exhibited the smallest particle size and only few agglomerates. Thus, the number of acid sites on the external zeolite surface is increased for HZSM-5 (25), leading to an improved accessibility of the acid sites and a lower temperature for hydrocarbon formation *via* the MtG process, accordingly. Higher reaction rates in the STD reaction have been described by Cai et al. for physically admixed STD catalysts containing zeolites with small particles sizes, however, no significant formation of hydrocarbons has been reported in this case.⁵⁴ While the number and strength of acid sites is important, the accessibility of these sites is also a crucial aspect in view of the catalytic properties of bifunctional catalysts.

3.2.4 Correlation of activity

A linear dependency of the catalyst activity on the Cu surface area has been reported for bifunctional STD catalysts.^{55,56} In this study, well-defined, uniform nanoparticles were used as catalyst precursors in order to avoid any effects of structure-sensitivity which has been proposed for methanol synthesis.^{57,58} Catalyst series based on the same acidic component thereby showed a linear dependency of CO conversion on the Cu loading (*e.g.*, HZSM-5 (140)-based samples at 250 °C), as long as DME was the main reaction product, clearly demonstrating the benefit of our uniform nanoparticle toolbox (Figure 1). Taking into account

all Cu/Zn/zeolite catalysts, a single materials descriptor, however, seems not to be sufficient to describe the catalyst behavior. According to our results, the ratio of the two catalytically active components as well as the accessibility (*e.g.*, micropore area) of the acid sites are crucial issues regarding catalyst activity. Therefore, the CO turnover rate was correlated with these parameters at 250 and 260 °C for all bifunctional, zeolite-based catalysts irrespective of the Si/Al ratio and the type of zeolite (Figure 6). For temperatures below 270 °C, an increase in the Cu to acid site ratio as well as a low micropore area resulted in an increase in turnover rate. For temperature above 270 °C, catalyst deactivation became more important.

Furthermore, an influence of the mixing ratio of the two catalytically active functions on the product spectrum of the hydrocarbons was observed. Figure 7 shows the fraction of C₁-C₄ hydrocarbons in those experiments, where DME was already consumed in favor of hydrocarbon formation. At 270 °C, CZ (9)-HZSM-5 (25) displayed the highest fraction of short chain hydrocarbons (78 %) and was the only bifunctional system showing a remaining DME selectivity of 17 %. If the number of acid sites was increased with respect to the amount of Cu in the bifunctional Cu/Zn/zeolite catalysts, the product spectrum was shifted towards lower hydrocarbons and the amount of C₁-C₄ components increased to 60-70 %. Depending on the desired product, LPG type compounds (in C₁-C₄ products) or C₅₊ compounds for fuel type applications can be produced in a single step.

For granular hybrid catalysts, the increased formation of methylated aromatics has been previously ascribed by Fujimoto et al. to the continuous formation of methanol over the entire catalyst bed, leading to the methylation of intermediates.⁴⁸ On the other hand, the product spectrum was shifted to lower alkanes with respect to the conventional MtG process for Cu/ZnO/ γ -Al₂O₃/HZSM-5 systems, which is in good agreement with our results.⁴⁹ The immediate hydrogenation of unsaturated intermediates was suggested to be responsible for this phenomenon as a consequence of the intimate contact between the two active components, whereby the formation of higher hydrocarbons and aromatics was reduced.

4. Conclusions

Bifunctional model catalysts were developed for the conversion of syngas to DME and hydrocarbons using the precursor concept. Well-defined and uniform Cu/Zn nanoparticles were prepared and successively immobilized on different dehydration catalysts to study the influence of the acidic properties on the catalytic performance. In particular, the Cu loading, the type of acidic sites (γ -Al₂O₃ vs. zeolites), the type of acid catalyst (HY vs. HZSM-5) and different Si/Al ratios were investigated.

Additionally, the formation of the active phase was monitored by *in situ* and *operando* XAS measurements. The Cu particles were completely reduced at 250 °C, also under reaction conditions at 3 bar, whereas the Zn prevailed as Zn²⁺. In agreement with *ex situ* XRD investigations of the catalysts after both calcination and catalytic testing, an amorphization of the ZnO phase was observed. The CO conversion was correlated with the ratio of the two catalytically active components and the micropore area of the bifunctional systems. With decreasing micropore area and increasing ratio of Cu to acidic sites, the CO conversion

increased. The overall DME synthesis rate was controlled by both the relative ratio of methanol synthesis to methanol dehydration components and the reaction conditions. The selectivity to LPG products was also controlled by the ratio of the two catalytically active components. Consequently, well-defined nanoparticle building units open an encouraging avenue for the preparation of bifunctional catalysts for conversion of synthesis gas to either DME or hydrocarbons, enabling further systematic studies of synthesis–structure–function relationships. Furthermore, by choosing different building blocks and systematic balancing of the two catalytic entities, future control of the product selectivities can be explored (*e.g.*, towards olefins, LPG or gasoline range products).

Acknowledgements

M.G. kindly acknowledges financial support of the Helmholtz Research School Energy-Related Catalysis. Further acknowledgments are given to the synchrotron radiation source at Karlsruhe Institute of Technology for providing beamtime at CAT-ACT beamline and Dr. Anna Zimina and Dr. Tim Prüßmann for their support during the measurements. Doreen Neumann-Walter and Dr. Thomas Otto are acknowledged for their support with the BET measurements.

References

- 1 N. Dahmen, E. Dinjus., *Chemie Ingenieur Technik*, 2010, **82**, 1147-1152.
- 2 E. Dinjus, U. Arnold, N. Dahmen, R. Höfer, W. Wach, *RCS Green Chemistry No. 4*, The Royal Society of Chemistry, London 2009, 125-163.
- 3 P. Lv, Z. Yuan, L. Ma, C. Wu, Y. Chen, J. Zhu, *Renewable Energy*, 2007, **32**, 2173-2185.
- 4 D. Mao, J. Xia, Q. Chen, G. Lu, *Catal. Commun.*, 2009, **10**, 620-624.
- 5 F. S. Ramos, A. M. Duarte de Farias, L. E. P. Borges, J. L. Monteiro, M. A. Fraga, E. F. Sousa-Aguiar, L. G. Appel, *Catalysis Today*, 2005, **101**, 39-44.
- 6 A. Mittasch, M. Pier, US 1569775 A, 1926
- 7 J.-D. Grunwaldt, A. M. Molenbroek, N.-Y. Topsoe, H. Topsoe, B. S. Clausen, *Journal of catalysis*, 2000, **194**, 452-460.
- 8 M. Behrens, R. Schlögl, *J. Anorg. Allg. Chem.*, 2013, **639**, 2683-2695.
- 9 S. Hassanpour, M. Taghizadeh, *Ind. Eng. Chem. Res.*, 2010, **49**, 4063-4069.
- 10 M. Stiefel, R. Ahmad, U. Arnold, M. Döring, *Fuel Process Technology*, 2011, **92**, 1466-1474.
- 11 J. Abu-Dahrieh, D. Rooney, A. Gouget, Y. Saih, *Chem. Eng. Journal*, 2012, **203**, 201-211.
- 12 J.-H. Kim, M. J. Park, S. J. Kim, O.-S. Joo, K.-D. Jung, *Appl. Catal. A: General*, 2004, **264**, 37-41.
- 13 T. Takeguchi, K.-I. Yanagisawa, T. Inui, M. Inoue, *Applied Catalysis A: General*, 2000, **192**, 201-209.
- 14 J. Sun, G. Yang, Y. Yoneyama, N. Tsubaki, *ACS Catalysis*, 2014, **4**, 3346-3356.
- 15 Q. Ge, Y. Huang, F. Qiu, S. Li, *Applied Catalysis A: General*, 1998, **167**, 23-30.
- 16 J.-L. Li, X.-G. Zhang, T. Inui, *Appl. Catal. A*, 1996, **147**, 23-33.
- 17 C. Zeng, J. Sun, G. Yang, I. Ooki, K. Hayashi, Y. Yoneyama, A. Taguchi, T. Abe, N. Tsubaki, *Fuel*, 2013, **112**, 140-144.
- 18 R. Ahmad, D. Schrempf, S. Behrens, J. Sauer, M. Döring, U. Arnold, *Fuel Cell Proc. Technol.* 2014, **121**, 38-46.
- 19 G. Ertl., D. Prigge, *J. Catal.*, 1983, **79**, 359-377.
- 20 H.-J. Freund, M. Bäumer, J. Libuda, T. Risse, G. Rupprechter, S. Shaikhutdinov, *Journal of Catalysis*, 2003, **216**, 223-235.
- 21 M. Boudart, *Topics in Catalysis*, 2000, **13**, 147-149.
- 22 S. Vukojevic, O. Trapp, J.-D. Grunwaldt, C. Kiener, F. Schüth, *Angew. Chem. Int. Ed.*, 2005, **44**, 7978-7981.
- 23 M. Simon, A. Mortreux, F. Petit, *J. Chem. Soc., Chem. Commun.*, 1988, 1445-1446.
- 24 M. K. Schröter, L. Khodeir, M. W. E. van den Berg, T. Hikov, M. Cokoja, S. Miao, W. Grünert, M. Muhler, R. A. Fischer, *Chem. Commun.*, 2006, 2498-2500.
- 25 S. Schimpf, A. Rittermaier, X. Zhang, Z.-A. Li, M. Spasova, M. W. E. van den Berg, M. Farle, Y. Wang, R. A. Fischer, M. Muhler, *ChemCatChem* 2010, **2**, 214-222.
- 26 N. J. Brown, A. García-Trenco, J. Weiner, E. R. White, M. Allinson, Y. Chen, P. P. Wells, E. K. Gibson, K. Hellgardt, M. S. P. Shaffer, C. K. Williams, *ACS Catal.*, 2015, **5**, 2895-2902.
- 27 H. Bönemann, R. M. Richards, *Eur. J. Inorg. Chem.* 2001, 2455-2480.
- 28 H. Bönemann, G. Braun, W. Brijoux, R. Brinkmann, A. Schulze Tilling, K. Seevogel, K. Siepen, *Journal of Organometallic Chemistry*, 1996, **520**, 143-162
- 29 M. Gentzen, W. Habicht, D. E. Doronkin, J.-D. Grunwaldt, J. Sauer, S. Behrens, *Catal. Sci. and Technol.*, 2016, **6**, 1054-1063.
- 30 A. Zimina, K. Dardenne, M.A. Denecke, D. E. Doronkin, E. Huttel, H. Lichtenberg, S. Mangold, T. Pruessmann, J. Rothe, Th. Spangenberg, R. Steininger, T. Vitova, H. Geckeis, J.-D. Grunwaldt, *Rev. Sci. Instrum.*, 2017, **88**, 113113.

- 31 J.-D. Grunwaldt, M. Caravati, S. Hannemann, A. Baiker, *Phys Chem Chem Phys.*, 2004, **6**, 3037–3047.
- 32 B. Ravel, M. Newville, *J. Synchrotron Radiat.*, 2005, **12**, 537–541.
- 33 J.J. Rehr, R.C. Albers, *Rev. Mod. Phys.*, 2000, **72**, 621–654.
- 34 C. Baerlocher, L. B. McCusker, D. H. Olson, *Atlas of zeolite framework types*, 6th revised version, Elsevier B. V., 2007, Amsterdam.
- 35 T. Lunkebein, J. Schumann, M. Behrens, R. Schlögl, M. G. Willinger, *Angew. Chem. Int. Ed.*, 2015, **54**, 4544–4548.
- 36 M. Turco, G. Bagnasco, U. Costantino, F. Marmottini, T. Montanari, G. Ramis, G. Busca, *Journal of Catalysis*, 2004, **228**, 43–55.
- 37 Y. Guo, W. Meyer-Zaika, M. Muhler, S. Vukojevic, M. Epple, *Eur. J. Inorg. Chem.* 2006, 4774–4781.
- 38 X.-J. Tang, J.-H. Fei, Z.-Y. Hou, X.-M. Zheng, H. Lou, *Energy & Fuels*, 2008, **22**, 2877–2884.
- 39 J. Agrell, K. Hasselbo, K. Jansson, S. G. Järas, M. Boutonnet., *Appl. Catal. A* 2001, **221**, 239–250
- 40 H. Wilmer, T. Genger, O. Hinrichsen, *Journal of Catalysis*, 2003, **215**, 188–198.
- 41 B. Lindström, L. J. Pettersson, P. G. Menon, *Applied Catalysis A: General*, 2002, **234**, 111–125.
- 42 J. Sun, G. Yang, Q. Ma, I. Ooki, A. Taguchi, T. Abe, Q. Xie, Y. Yoneyama, N. Tsubaki, *J. Mater. Chem. A*, 2014, **2**, 8637–8643.
- 43 S. Kattel, P. J. Ramírez, J. G. Chen, J. A. Rodriguez, P. Liu, *Science*, **355**, 1296–1299.
- 44 Z. Zhu, A. Chutia, R. Sahnoun, M. Koyama, H. Tsuboi, N. Hatakeyama, A. Endou, H. Takaba, M. Kubo, C. A. Del Carpio, A. Miyamoto, *Japanese Journal of Applied Physics*, 2008, **47**, 2999–3006.
- 45 P. Vesborg, I. Chorkendorff, I. Knudsen, O. Balmes, J. Nerlov, A. M. Molenbroek, B. Clausen, S. Helveg, *J. Catal.*, 2009, **262**, 65–72.
- 46 J. H. Flores, M. I. P. da Silva, *Colloids and Surfaces A: Physicochem. Eng. Aspects*, 2008, **322**, 113–123.
- 47 V.V. Ordonsky, M. Cai, V. Sushkevich, S. Moldovan, O. Ersen, C. Lancelot, V. Valtchev, A.Y. Khodakov, *Applied Catalysis A: General*, 2014, **486**, 266–275.
- 48 K. Fujimoto, K. Asami, H. Saima, T. Shikada, H. Tominaga, *Ind. Eng. Chem. Prod. Res. Dev.*, 1986, **2**, 262–267.
- 49 E. Lorenz, P. Wehling, M. Schlereth, B. Kraushaar-Czarnetzki, *Catalysis Today*, 2016, **275**, 183–190.
- 50 R. Choudry, T. Mandal, *Fuel Science and Technology International*, 1990, **8**, 1021–1036.
- 51 C. D. Chang, *Catalysis Reviews*, 1983, **25**, 1–118.
- 52 Y. Liu, S. Müller, D. Berger, J. Jelic, K. Reuter, M. Tonigold, M. Sanchez-Sanchez, J. A. Lercher, *Angew. Chem. Int. Ed.*, 2016, **55**, 5723–5726.
- 53 J.-H. Kim, M. J. Park, S. J. Kim, O.-S. Joo, K.-D. Jung, *Appl. Catal. A: General*, 2004, **264**, 37–41.
- 54 M. Cai, A. Palčić, V. Subramanian, S. Moldovan, O. Ersen, V. Valtchev, V.V. Ordonsky, A.Y. Khodakov, *J. Catal.*, 2016, **338**, 227–238.
- 55 M. Kurtz, H. Wilmer, T. Genger, O. Hinrichsen, M. Muhler, *Catal. Lett.*, 2003, **86**, 77–80
- 56 J. Robbins, E. Iglesia, C.P. Kelkar, B. DeRites, *Catal. Lett.*, 1991, **10**, 1–10.
- 57 J. Yoshihara, C. T. Campbell, *Journal of Catalysis*, 1996, **161**, 776–782.
- 58 H. Wilmer, M. Kurtz, K. V. Klementiev, O. P. Tkachenko, W. Grünert, O. Hinrichsen, A. Birkner, S. Rabe, K. Merz, M. Driess, C. Wöll, M. Muhler, *Phys. Chem. Chem. Phys.*, 2003, **5**, 4736–4742.



Figure 1. Preparation of bifunctional catalysts for syngas conversion using nanoparticle building units.

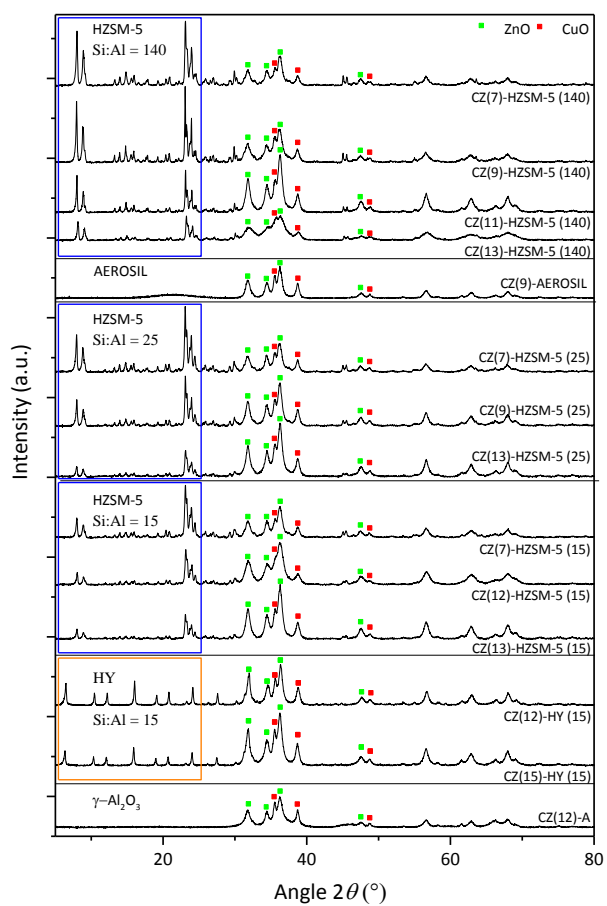


Figure 2. XRD patterns of the bifunctional catalysts after calcination.

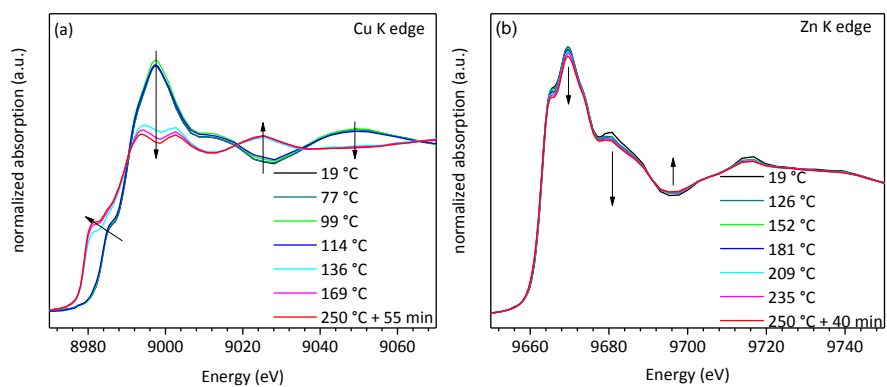


Figure 3. *In situ* XANES spectra at the Cu K (a) and the Zn K edge (b) of CZ (12)-A between 25 and 250 °C in 5 % H₂ in He.

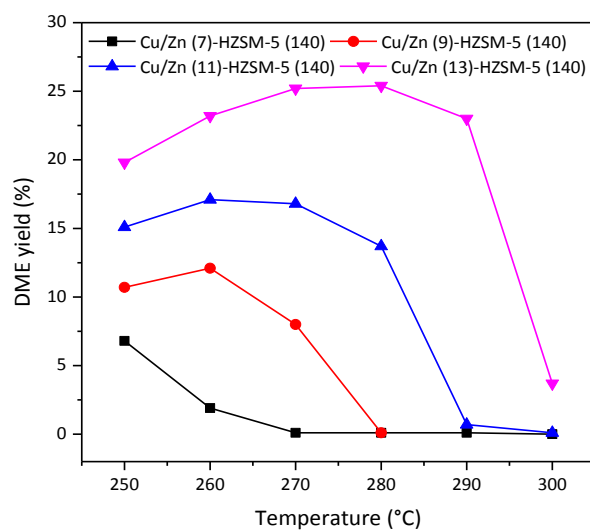


Figure 4. Effect of Cu loading on the DME yield for HZSM-5 (140)-based catalysts.

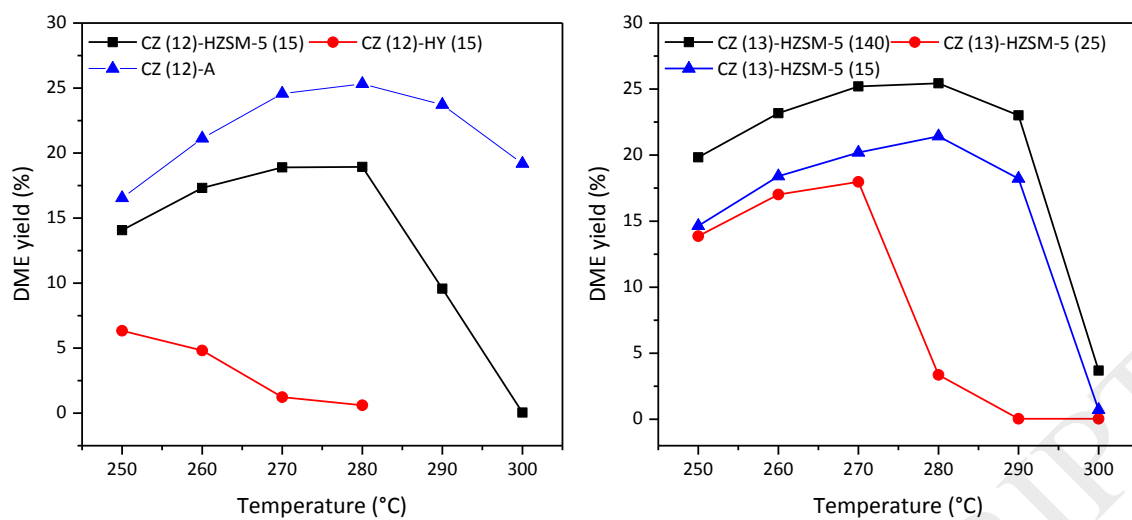


Figure 5. DME yields of bifunctional catalysts with (left) 12 wt.-% Cu loading and (right) 13 wt.-% Cu-loading.

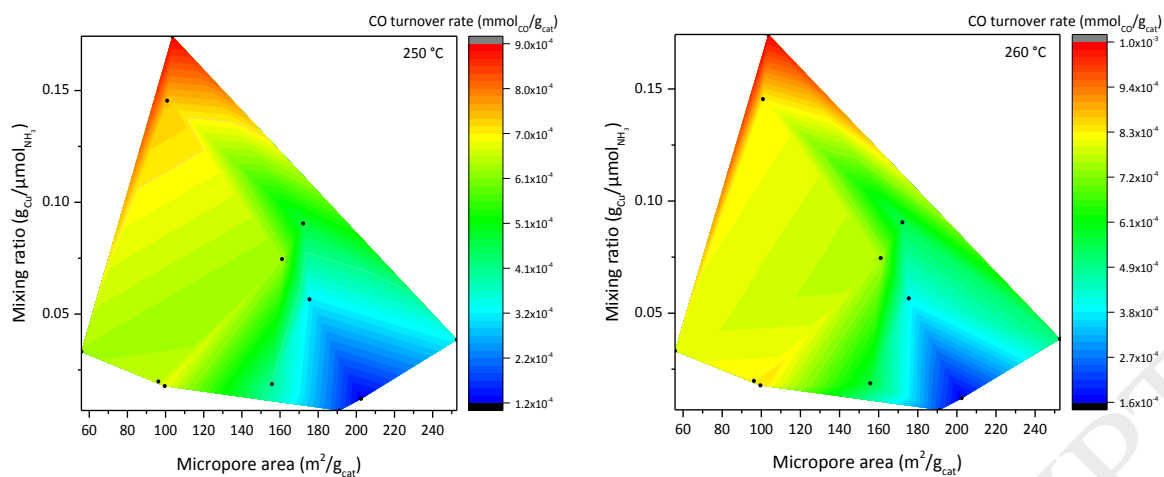


Figure 6. Specific CO turnover rates and ratio of the two catalytically active components in the bifunctional catalyst as a function of the micropore area (left) at 250 °C and (right) at 260 °C.

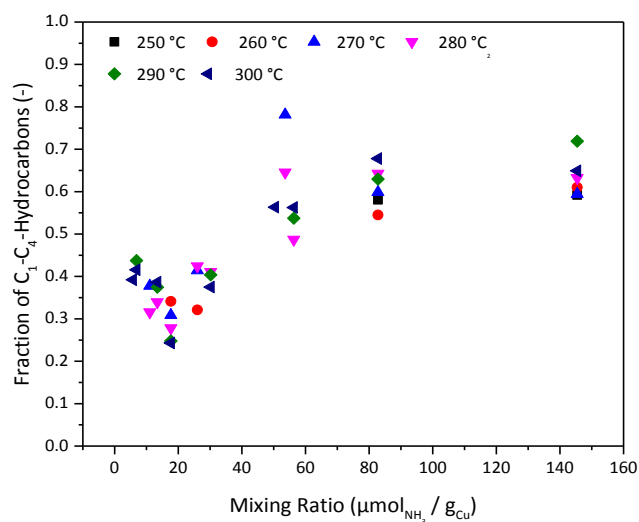


Figure 7. Influence of the ratio of the two catalytically active components in the bifunctional catalysts on the formation of light hydrocarbons (*i.e.*, fraction of C₁-C₄ hydrocarbons in organic product) in the direct conversion of synthesis gas for a temperature range of 250 °C to 300 °C.

Table 1. Compositions and specific surface areas of the bifunctional model catalysts

Catalyst	w_{Cu} (%)	w_{Zn} (%)	A_{BET} (m²/g)	A_{calculate} d (m²/g)
CZ (7)-HZSM-5 (140)	7.1	17.6	269.6	263.1
CZ (9)-HZSM-5 (140)	9.6	24.5	243.8	227.0
CZ (11)-HZSM-5 (140)	11.2	35.3	190.1	172.8
CZ (13)-HZSM-5 (140)	13.2	34.7	150.4	170.5
CZ (9)-AEROSIL	9.3	21.9	84.1	-
CZ (7)-HZSM-5 (25)	7.5	21.0	253.7	249.0
CZ (9)-HZSM-5 (25)	9.7	27.5	207.7	225.7
CZ (13)-HZSM-5 (25)	12.9	33.5	154.0	176.5
CZ (7)-HZSM-5 (15)	7.7	19.9	243.8	264.5
CZ (12)-HZSM-5 (15)	12.2	34.2	161.5	173.7
CZ (13)-HZSM-5 (15)	13.5	38.2	144.0	176.5
CZ (12)-H-Y (15)	11.9	33.1	305.2	311.0
CZ (16)-H-Y (15)	15.6	39.8	214.6	219.9

Table 2. Results of the NH₃-TPD experiments.

Catalyst	NH ₃ desorbed ($\mu\text{mol}/\text{g}_{\text{cat}}$)	Amount of strong acid sites ($> 500\text{ }^\circ\text{C}$) (%)	Calculated NH ₃ - amount ($\mu\text{mol}/\text{g}_{\text{cat}}$)
HZSM-5 (140)	99.1	3.0	-
HZSM-5 (25)	521.8	9.1	-
HZSM-5 (15)	890.9	10.2	-
HY	411.4	8.1	-
$\gamma\text{-Al}_2\text{O}_3$	182.1	-	-
AEROSIL	0	-	-
CZ (7)-HZSM-5 (140)	144.8	11.7	125.5
CZ (9)-HZSM-5 (140)	146.6	10.1	137.8
CZ (11)-HZSM-5 (140)	139.9	9.3	137.3
CZ (13)-HZSM-5 (140)	94.4	10.3	154.3
CZ (9)-AEROSIL	81.9	3.8	-
CZ (7)-HZSM-5 (25)	432.6	21.5	376.4
CZ (9)-HZSM-5 (25)	363.8	17.4	345.3
CZ (13)-HZSM-5 (25)	274.0	14.8	308.3
CZ (7)-HZSM-5 (15)	625.9	14.7	627.7
CZ (12)-HZSM-5 (15)	425.5	11.3	450.9
CZ (13)-HZSM-5 (15)	345.7	13.7	402.5
CZ (12)-H-Y (15)	339.6	4.4	259.4
CZ (16)-H-Y (15)	245.6	5.7	242.3
CZ (12)-A	163.0	-	181.6

59
60